Berry phase engineering at oxide interfaces

D. J. Groenendijk,[1,*] C. Autieri,[2,3,*] T. C. van Thiel,[1,*,†] W. Brzezicki,[2,3,*] J. R. Hortensius,[1] D. Afanasiev,[1] N. Gauquelin,[4] P. Barone,[2] K. H. W. van den Bos,[4] S. van Aert,[4] J. Verbeeck,[4] A. Filippetti,[5,6] S. Picozzi,[2] M. Cuoco,[2,7,‡] and A. D. Caviglia[1,§]

[1]*Kavli Institute of Nanoscience, Delft University of Technology, P.O. Box 5046, 2600 GA Delft, Netherlands*
[2]*Consiglio Nazionale delle Ricerche, CNR-SPIN, Italy*
[3]*International Research Centre MagTop, Institute of Physics, Polish Academy of Sciences, Aleja Lotników 32/46, PL-02668 Warsaw, Poland*
[4]*Electron Microscopy for Materials Science (EMAT), University of Antwerp, 2020 Antwerp, Belgium*
[5]*Dipartimento di Fisica, Università di Cagliari, Cagliari, Monserrato 09042-I, Italy*
[6]*CNR-IOM, Istituto Officina dei Materiali, Cittadella Universitaria, Cagliari, Monserrato 09042-I, Italy*
[7]*Dipartimento di Fisica "E. R. Caianiello" Università degli Studi di Salerno, 84084 Fisciano, Italy*

(Received 15 January 2020; revised manuscript received 3 April 2020; accepted 11 May 2020; published 25 June 2020)

Three-dimensional strontium ruthenate ($SrRuO_3$) is an itinerant ferromagnet that features Weyl points acting as sources of emergent magnetic fields, anomalous Hall conductivity, and unconventional spin dynamics. Integrating $SrRuO_3$ in oxide heterostructures is potentially a novel route to engineer emergent electrodynamics, but its electronic band topology in the two-dimensional limit remains unknown. Here we show that ultrathin $SrRuO_3$ exhibits spin-polarized topologically nontrivial bands at the Fermi energy. Their band anticrossings show an enhanced Berry curvature and act as competing sources of emergent magnetic fields. We control their balance by designing heterostructures with symmetric ($SrTiO_3/SrRuO_3/SrTiO_3$ and $SrIrO_3/SrRuO_3/SrIrO_3$) and asymmetric interfaces ($SrTiO_3/SrRuO_3/SrIrO_3$). Symmetric structures exhibit an interface-tunable single-channel anomalous Hall effect, while ultrathin $SrRuO_3$ embedded in asymmetric structures shows humplike features consistent with multiple Hall contributions. The band topology of two-dimensional $SrRuO_3$ proposed here naturally accounts for these observations and harmonizes a large body of experimental results.

DOI: 10.1103/PhysRevResearch.2.023404

I. INTRODUCTION

In topologically nontrivial band structures, electrons acquire an additional phase factor when their wave functions traverse a closed loop in momentum space [1]. Although this concept is now commonly referred to as the Berry phase mechanism, Karplus and Luttinger already demonstrated decades earlier that the anomalous Hall effect—which is prevalent in itinerant ferromagnets—finds its origins in band topology [2]. In addition to the usual band dispersion contribution, electrons in an electric field $\boldsymbol{\mathcal{E}}$ acquire an anomalous velocity:

$$\boldsymbol{v}(\boldsymbol{k}) = \frac{1}{\hbar}\frac{\partial \boldsymbol{E}(\boldsymbol{k})}{\partial \boldsymbol{k}} - \frac{e}{\hbar}\boldsymbol{\mathcal{E}} \times \boldsymbol{b}(\boldsymbol{k}), \tag{1}$$

where $E(\boldsymbol{k})$ is the dispersion relation and $\boldsymbol{b}(\boldsymbol{k})$ is the momentum-space Berry curvature. The latter term describes the nontrivial geometry of the band structure and acts as an effective magnetic flux, which generally underlies topological transport phenomena such as the quantum, spin, and anomalous Hall effect (AHE) [1–5]. The anomalous velocity is transverse to the electric field and gives rise to a Hall current, with a sign and magnitude that depend sensitively on the band structure topology. In systems with ferromagnetic order and sizable spin-orbit coupling (SOC), the Berry curvature is strongly enhanced near avoided band crossings, which act as a source or sink of the emergent magnetic field [6]. A prototypical system is the transition-metal oxide $SrRuO_3$ (SRO), a 4*d* itinerant ferromagnet [7]. Its anomalous Hall conductivity in the bulk depends sensitively on the magnetization and on the position of the Fermi energy with respect to the Weyl points in the three-dimensional (3D) electronic spectra [5,8–10]. Extrinsic (scattering) mechanisms are known to contribute to the AHE in SRO [11–13]. However, when the Weyl points are in close proximity to the Fermi energy the intrinsic Berry curvature mechanism becomes dominant [10], particularly at temperatures far below the Curie point [5,11]. The Berry curvature is particularly sensitive to electronic reconstructions. Accordingly, integrating ultrathin SRO within heterostructures is a promising route to engineer topological transport phenomena. A suitable material for this purpose is $SrIrO_3$ (SIO), a 5*d* paramagnetic semimetal with strong atomic SOC (∼0.4 eV) [14–18] and excellent structural compatibility with SRO.

*These authors contributed equally to this work.
†t.c.vanthiel@tudelft.nl
‡mario.cuoco@spin.cnr.it
§Corresponding author: a.caviglia@tudelft.nl

Published by the American Physical Society under the terms of the Creative Commons Attribution 4.0 International license. Further distribution of this work must maintain attribution to the author(s) and the published article's title, journal citation, and DOI.

Recently, the behavior and control of the AHE in SRO ultrathin films and heterostructures have been at the center of intense research [19–28], fueled by the observation of humplike features in the transverse resistivity [29]. Such features are generally considered to be a manifestation of the topological Hall effect (THE). In this scenario, noncollinear spin textures give rise to Berry curvature sources in real space [30–32]. Embedding SRO in $SrTiO_3$ (STO) and $SrIrO_3$ (SIO) heterostructures (SIO/SRO/STO) sets a favorable environment for nontrivial spin textures (e.g., skyrmions) because of the strong SOC present in SIO and the breaking of inversion symmetry [19,29]. Moreover, humplike features in the Hall response have also been observed in SRO thin films interfaced with STO and vacuum [33–37], pointing to an important role played by asymmetric boundary conditions and momentum-space sources of Berry curvature. Despite a number of seminal contributions, a unifying scheme is still lacking. In this work we perform a theoretical analysis of the low-energy electronic structure and band topology of SRO in the two-dimensional limit. We reveal spin-polarized topologically nontrivial bands at the Fermi energy, associated with sources of Berry curvature, bringing about competing contributions to the anomalous Hall response. We subsequently use these insights to investigate theoretically and experimentally the AHE in ultrathin SRO films with (a)symmetric boundary conditions. Our results highlight the importance of momentum-space Berry curvature contributions, in addition to the real-space sources discussed so far.

The remainder of the article is organized as follows; in Sec. II we present the methodology regarding the density function theory (DFT) calculations, sample fabrication, and the structural and magnetotransport characterization. Section III is devoted to the main results; (1) the Hall effect measurements in symmetric and asymmetric heterostructures (SRO interfaced with SIO and STO) and (2) the theoretical calculations of the Hall conductivity, combining DFT and effective tight-binding modeling for the designed heterostructures. Section IV contains a discussion and concluding paragraph.

II. METHODS

A. Density functional theory calculations

First-principles DFT calculations were performed using the VASP [38] package based on plane-wave basis set and projector augmented wave method [39]. A plane-wave energy cutoff of 500 eV was used. For the treatment of the exchange-correlation, the LSDA (local spin density approximation) with the Perdew-Zunger [40] parametrization of the Ceperly-Alder data [41] for the exchange-correlation functional was considered. The choice of the LSDA exchange functional is suggested by Etz *et al.* [42], where it was shown that the LSDA is a better approximation than the generalized gradient approximation for bulk SRO and its heterostructures [43,44]. In our simulations, the STO/SRO/SIO heterostructure was constructed using a lateral supercell of $\sqrt{2}a \times \sqrt{2}a$, while the phases without rotations were contracted using a lateral supercell of $a \times a$. The in-plane lattice parameter was fixed to the STO substrate, while for the out-of-plane lattice parameters the experimental values of the single unit cell of SRO and SIO were used. The hopping parameters were estimated from the electronic structure of the nonmagnetic SRO/SIO and SRO/STO interfaces without Coulomb repulsion. After obtaining the Bloch wave functions from DFT, the maximally localized Wannier functions [45,46] were constructed using the WANNIER90 code [47]. Starting from an initial projection of atomic d-basis functions belonging to the t_{2g} manifold and centered on metal sites, the t_{2g}-like Wannier functions were obtained. To extract the hopping parameters from the electronic bands at low energies, the Slater-Koster interpolation, as implemented in WANNIER90, was used. This approach is applied to determine the real space Hamiltonian matrix elements in the t_{2g}-like Wannier function basis for the SRO/SIO and SRO/STO interfaces.

B. Sample fabrication

SRO/STO, SRO/SIO/STO, and SIO/SRO/SIO/STO heterostructures were prepared by pulsed laser deposition on TiO_2-terminated STO(001) substrates. The films were deposited at 600 °C in an oxygen pressure of 0.1 mbar. The laser fluence was 1.2 J/cm^2 and the repetition rate was 1 Hz. The samples were annealed at 550 °C in an oxygen pressure of 300 mbar and cooled down in the same pressure at a rate of 20 °C/min. The growth was monitored by reflection high-energy electron diffraction (RHEED), indicating a layer-by-layer growth mode for all three materials.

C. Structural and magnetotransport characterization

Atomic scale characterization of the lattice structure was performed on an aberration corrected STEM. The FEI Titan 80-300 microscope was operated at 300 kV and the samples were prepared in a vacuum transfer box and analyzed in a Gatan vacuum transfer holder to avoid any influence of air on the film [48,49]. Collection angles for HAADF imaging, ABF imaging, and EELS were 44–190, 8–17, and 47 mrad, respectively. The STEM-EELS measurements show that there is negligible diffusion of Ru and Ti, whereas there is a measurable diffusion of Ir into the top RuO_2 layer. The heterostructures were further investigated by synchrotron x-ray diffraction measurements and atomic force microscopy (see Sec. I A of the Supplemental Material [50]). Hall bars were patterned by e-beam lithography and the heterostructure was contacted by Ar milling and *in situ* deposition of Pd and Au, resulting in low resistance Ohmic contacts. An STO capping layer was used to impose symmetric boundary conditions or to prevent degradation of the SIO layer [17,18,51]. Transport measurements were performed in a He flow cryostat with a 10 T superconducting magnet and a base temperature of 1.5 K. Measurements in current-bias configuration were performed by sourcing a low frequency (∼17 Hz) 10 μA current and measuring the resulting (longitudinal and transverse) voltage drop with a lock-in amplifier.

III. RESULTS

We first analyze theoretically the properties of ultrathin SRO, starting from the Ru-based t_{2g} electronic structure close to the Fermi level. Our *ab initio* derived tight-binding

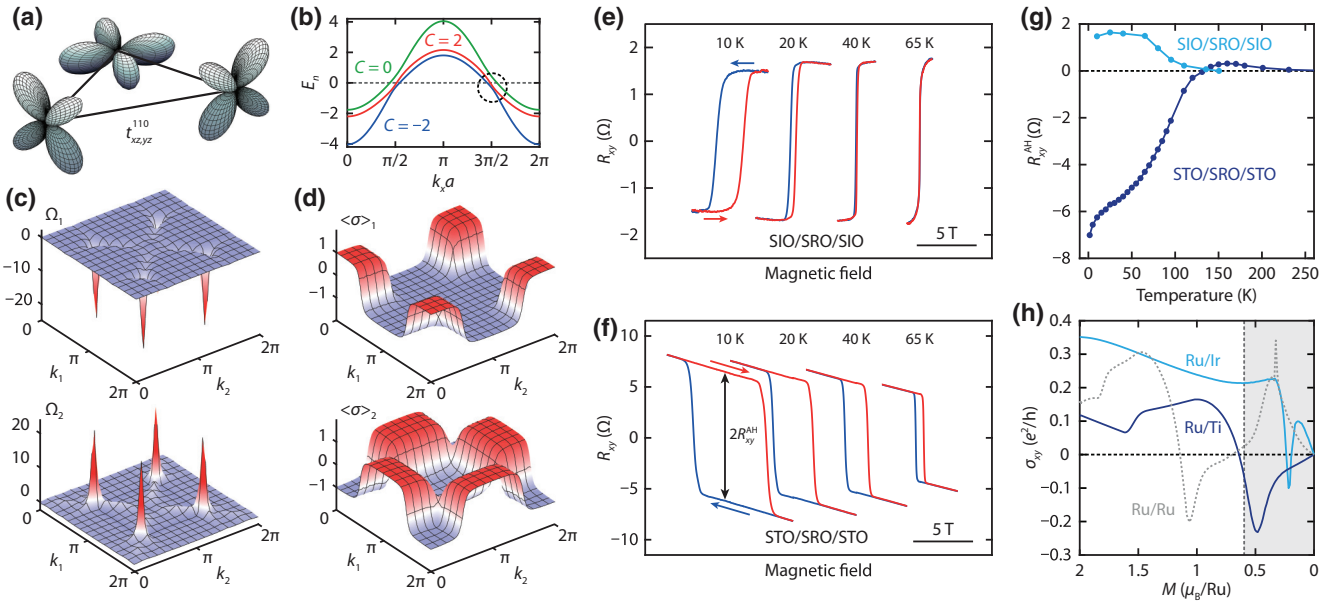

FIG. 1. Anomalous Hall effect of ultrathin SRO with symmetric boundary conditions. (a) Next-nearest-neighbor interorbital hopping. (b) Dispersion of Ru t_{2g} bands along $k_x = k_y$ for a representative value of the magnetization (see Sec. V B of the Supplemental Material [50]). (c) Berry curvature associated with topologically nontrivial Ru t_{2g} bands close to the Fermi level (Chern numbers $\mathcal{C} = \pm 2$). (d) Spin polarizations $\langle \sigma^z \rangle_n$ for the corresponding bands. (e) and (f) Hall resistance of symmetric SIO/SRO/SIO (e) and STO/SRO/STO (f) heterostructures as function of temperature. The curves are offset horizontally. (g) Temperature evolution of the amplitude of the AHE (R_{xy}^{AH}). (h) Evolution of the intrinsic contribution to σ_{xy} for Ru/Ti, Ru/Ir, and Ru/Ru bilayers as a function of the average Ru magnetization. The dashed black line indicates the approximate saturated magnetization value of the STO/SRO/SIO determined from SQUID measurements.

calculations show that the Berry curvature of the individual bands is strongly enhanced at avoided band crossings due to next-nearest-neighbor interorbital hopping [Fig. 1(a)] in the presence of SOC. We first focus on the monolayer SRO system. Its electronic structure can be arranged in two groups of three bands with different spin-orbital parity. Within each sector there are two topologically nontrivial bands carrying a Chern number $\mathcal{C} = \pm 2$, accompanied by a single, trivial band with $\mathcal{C} = 0$ [see Fig. 1(b)]. The ensuing Berry curvature of the nontrivial bands, which have a predominantly d_{xz} and d_{yz} character, is shown in Fig. 1(c). We find sharp peaks located at the avoided bands crossings. Since the lowest energy bands in Fig. 1(b) have a nontrivial Chern number, the Berry curvature contribution of each band cannot vanish and is robust to changes in the Fermi level or, in general, of the corresponding electron occupation. Their splitting and relative occupation leads to a dominance of one of the contributions, including sign changes when considering the averaged Berry curvature. A complete compensation is improbable and can only occur by electronic fine tuning. SOC influences the character of the avoided crossings and causes the bands with opposite Berry curvature and $d_{xz/yz}$ orbital character to have a distinct momentum dependence of the spin polarization, with an opposite sign developing nearby the points of maximal Berry curvature accumulation, as shown in Fig. 1(d).

We now investigate SRO films with symmetric boundary conditions, shown in Figs. 1(e)–1(g). We consider heterostructures composed of STO/2 u.c. SIO/4 u.c. SRO/2 u.c. SIO/10 u.c. STO and STO/4 u.c. SRO/10 u.c. STO. Detailed information regarding the synthesis and characterization of all samples is provided in the Supplemental Material [50]. Strikingly, we find that the sign of the AHE is opposite for SIO/SRO/SIO [Fig. 1(e)] and STO/SRO/STO [Fig. 1(f)] heterostructures. This immediately shows that symmetry breaking in ultrathin SRO directly controls the magnitude and sign of the Berry curvature. The magnitude of the AHE (R_{xy}^{AH}) as a function of temperature is shown in Fig. 1(g). While R_{xy}^{AH} of the STO/SRO/STO is mainly negative and changes sign near the Curie temperature (T_{C}), R_{xy}^{AH} of the SIO/SRO/SIO remains positive in the entire temperature range. This confirms the expectation that the occupation of the topologically active Ru t_{2g} bands depends sensitively on the electronic and magnetic reconstruction at the interface. This behavior can be qualitatively captured by modeling Ru/Ti and Ru/Ir bilayers, i.e., systems with a single u.c. of SRO coupled to a single u.c. of STO or SIO. As shown in Fig. 1(h), for small/intermediate amplitude of the Ru magnetization the AH conductivity is negative for the Ru/Ti bilayer, while it is positive for the Ru/Ir bilayer. In the former, only the Ru $d_{xz,yz}$ contribute since the STO is electronically inert, while for the latter, the intrinsic competition of the topological Ru bands is modified through the hybridization of the Ir/Ru $d_{xz,yz}$ orbitals, and interfacial magnetic canting/reconstruction.

To study the effect of asymmetric boundary conditions, we now investigate the tricolor STO/SRO/SIO system (Fig. 2). Given the different trends observed in the symmetric systems, we expect competition in the total R_{xy}^{AH} in this case. The atomic arrangement at the interfaces is investigated by high-angle annular dark-field scanning transmission electron microscopy (HAADF-STEM) [Fig 2(b)]. Chemical analysis by electron

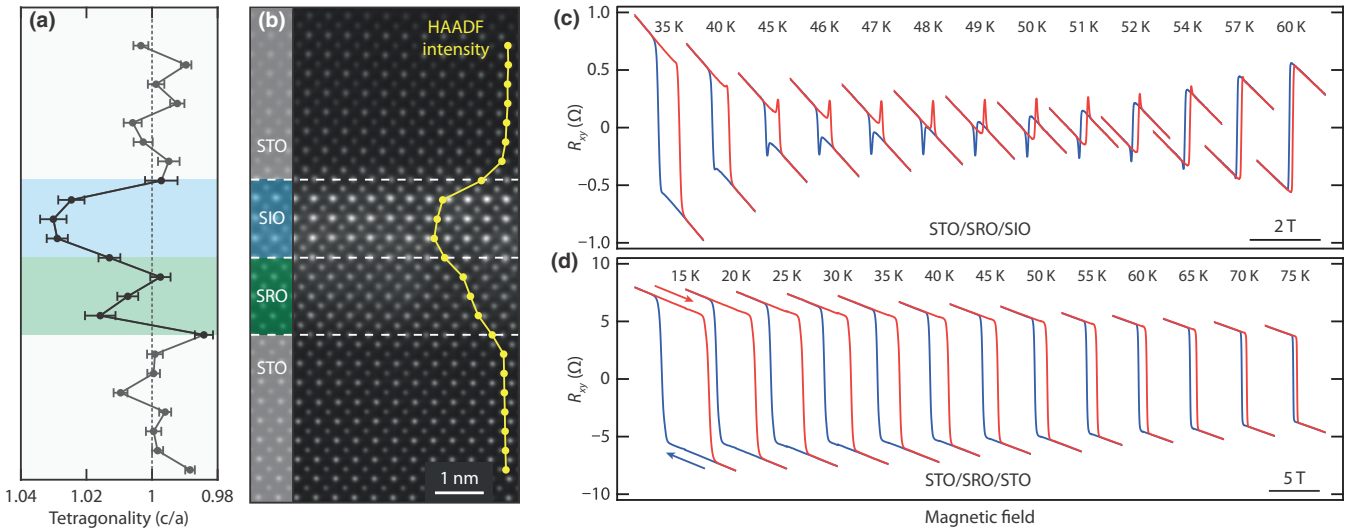

FIG. 2. Anomalous Hall effect of ultrathin SRO heterostructures with asymmetric boundary conditions. (a) Mean tetragonality of the perovskite unit cell across the heterostructure. (b) HAADF-STEM measurement of a STO/SRO/SIO heterostructure. (c) and (d) Measured Hall resistance of (c) an asymmetric STO/SRO/SIO heterostructure and (d) a symmetric STO/SRO/STO heterostructure as function of temperature. The curves are offset horizontally.

energy loss spectroscopy (EELS) shows that the Ti/Ru and Ti/Ir interfaces are atomically sharp, while at the Ru/Ir interface there is a diffusion of Ir into the topmost RuO_2 layer. In addition, the thicknesses of both the SRO and SIO layers are 4 u.c. as designed (see also Sec. I C of the Supplemental Material [50]). After quantifying atomic column positions in the HAADF-STEM image using StatSTEM [52], a detailed analysis of the atomic positions shows that octahedral tilts are suppressed and both the SRO and SIO tend to a tetragonal rather than an orthorhombic symmetry as in their bulk form. In addition, we find that the tetragonality (c/a ratio) of the unit cell varies strongly across the SRO and SIO layers [Fig. 2(a)]. Since the magnetic anisotropy of SRO is known to be sensitive to strain and tetragonality [53–55], this affects the easy axis direction of the different SRO layers and hence the local magnetization of the Ru atoms. Theoretical calculations with multilayer configurations corresponding to the designed heterostructures show that the temperature dependent sign change of the AHE is well reproduced by the combined *ab initio* and tight-binding modeling (see Sec. V D of the Supplemental Material [50]). Furthermore, we demonstrate that the reversal temperature and amplitude of the AH conductance in the asymmetric heterostructure should generally depend on the magnetic proximity and anisotropy at the SRO/SIO interface. The AHE of the asymmetric STO/SRO/SIO is shown in Fig. 2(c). With increasing temperature, the AHE changes sign at the reversal temperature $T_R = 48$ K and peaks appear to be superimposed on the Hall effect, slightly above or below the coercive field (B_c). This is in stark contrast with the AHE of an STO/SRO/STO heterostructure [Fig. 2(d)], where the magnitude (R_{xy}^{AH}) decreases with increasing temperature. The peaks seemingly superimposed on the Hall effect are present between 35 and 58 K and reach their maximum amplitude at T_R, i.e., when R_{xy}^{AH} appears to be zero. This strongly suggests that their occurrence can be intrinsically linked to the sign reversal of the AHE. In the following we will explore this concept further.

Having assessed the sign tunability of the AHE in symmetric STO/SRO/STO, SIO/SRO/SIO heterostructures as a consequence of intrinsic contributions due to the topological nontrivial character of the Ru t_{2g} bands in ultrathin SRO, we consider the anomalies of the Hall resistivity in asymmetric STO/SRO/SIO. To move further into this analysis, aided by *ab initio* and tight-binding calculations, it is natural to expect that the resulting AHE in the designed heterostructures can be considered as a superposition of AH channels with opposite sign and suitable weights [56–58]. Indeed, the data are well described by two such channels, each having a slightly different coercive field [see Fig. 3(a)]. When a current is applied in the plane of the heterostructure and an out-of-plane magnetic field is varied in the range $[0, B, -B, 0]$, the total AHE is given by the sum of the AHE of the two contributions (this assumption is valid for small Hall angles, which is appropriate for SRO [28], see also Sec. II F of the Supplemental Material [50]). Depending on their relative magnitudes, three different behaviors can be discerned for $B_{c,II} < B_{c,I}$. In Fig. 3(b) we present a sketch of the corresponding real-space picture. For opposite signs of the anomalous amplitude, majority spin is accumulated on opposite terminals, resulting in opposite Hall voltages. When the anomalous amplitudes are equal in magnitude, the total AHE reduces to zero. In Fig. 3(c) the ordinary Hall component has been subtracted and the remaining anomalous Hall component (R_{AH}) is presented. As the temperature is increased from 46 K towards 51 K, the behavior of the total AHE evolves from the leftmost scenario in Fig. 3(a) to the rightmost scenario, with the middle scenario emerging at $T_R = 48$ K. Accordingly, we fit the experimental data with two oppositely oriented AHE loops, as $R_{AH} = R_{xy,I}^{AH} \tanh[\omega_I(B - B_{c,I})] + R_{xy,II}^{AH} \tanh[\omega_{II}(B - B_{c,II})]$, where ω is a parameter describing the slope at B_c. An excellent agreement is obtained between this model [dashed black lines in Fig. 3(b)] and the data, enabling us to extract the individual AH components as a function of temperature [Fig. 3(d)]. The corresponding R_{xy}^{AH} values are shown in Fig. 3(e); both

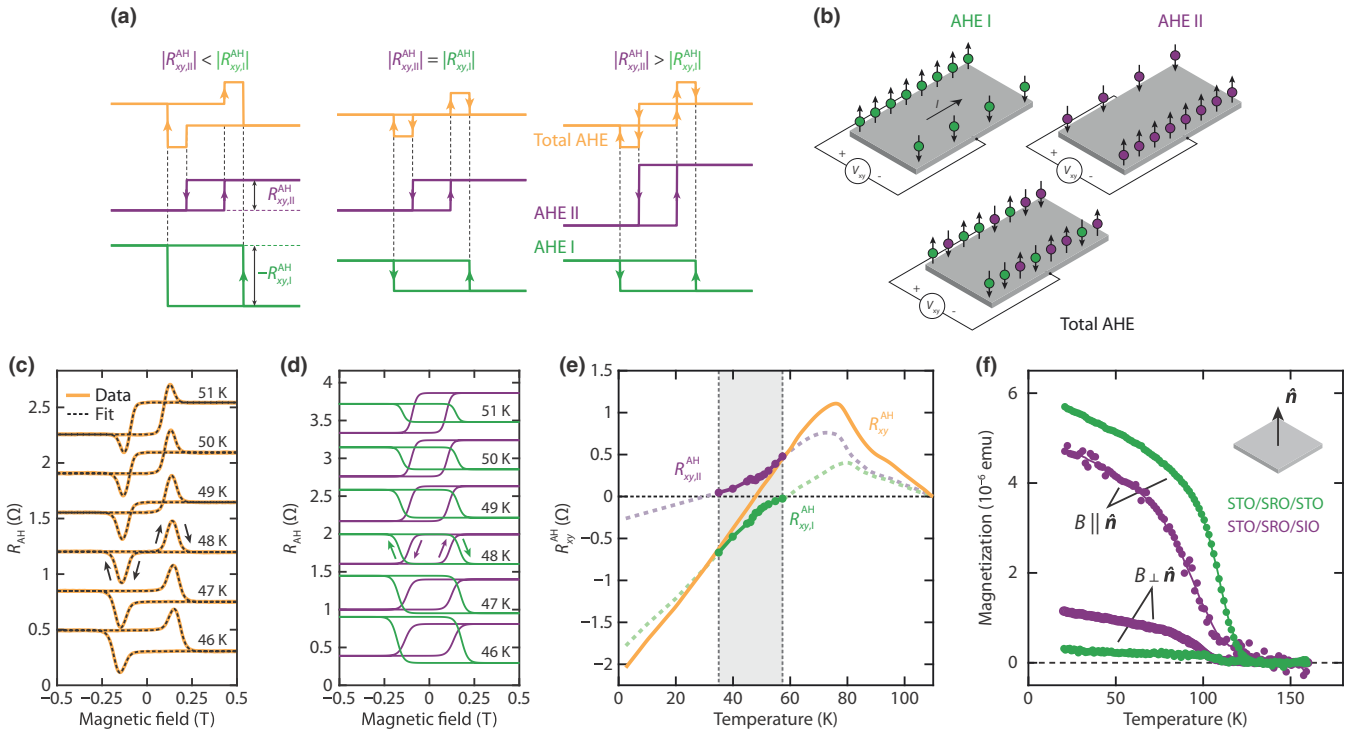

FIG. 3. Double AHE model. (a) Addition of two AHE contributions with opposite sign of R_{xy}^{AH}. (b) Illustration showing the opposite spin accumulation of the two individual contributions. (c) Measured total AHE curves with the ordinary Hall component subtracted. The black dashed lines represent a fit to two individual loops. (d) The two anomalous Hall components that add up to the total R_{AH} curves in (c). (e) Total R_{xy}^{AH} and the extracted R_{xy}^{AH} from the two anomalous Hall components as a function of temperature. The dashed lines illustrate a possible temperature dependence of R_{xy}^{AH}. (f) In- and out-of-plane magnetization for an (green) STO/SRO/STO and (purple) STO/SRO/SIO heterostructure, measured by SQUID.

components show a smooth evolution in temperature, with one disappearing above 58 K (green) and the other below 35 K (purple). At 48 K the two components are equal, leading to the fully compensated case. The dashed lines illustrate a possible dependence of $R_{xy}^{\mathrm{AH}}(T)$ at higher and lower temperatures, which suggests that R_{xy}^{AH} and B_{c} of the two contributions follow a qualitatively similar temperature dependence, shifted by 23 K. This implies that, for $T < 35$ K and $T > 58$ K, R_{xy}^{AH} of the two contributions are of the same sign or the positive contribution is below the detection limit of our experiment, rendering the total AHE indistinguishable from that of a single spin-polarized contribution (see Sec. II D of the Supplemental Material [50]). We note that that any two curves that add up to the total R_{xy}^{AH} are in principle possible.

There are various observations to be made concerning the relationship between the emergence of two opposite sign AH channels and the role of (in- and out-of-plane) inhomogeneities in the magnetization. First, we point out that the magnetic anisotropy is strongly affected by asymmetric boundary conditions. Figure 3(f) compares the in- and out-of-plane magnetization for an STO/SRO/STO and STO/SRO/SIO heterostructure. We observe that at SRO/SIO interfaces, the out-of-plane component of the magnetization is reduced and an in-plane component emerges. Considering the tetragonality profile discussed in Fig. 2(a), a nonuniform magnetization along the growth axis is expected, giving rise to the emergence of two opposite AH channels as two effective layers. The impact of an inhomogeneous magnetic anisotropy is also deduced from the theoretical calculations performed for an asymmetric STO/SRO/SIO heterostructure with 4 u.c. SRO (see Fig. S20 in the Supplemental Material [50]). Second, we note that an in-plane distribution of coercive fields may also play a role. In this scenario, the plane would be broken up into various domains with different switching fields and different AHE amplitudes. The agreement of the data with the double AHE model then suggests a bimodal distribution of switching fields [Figs. 4(a) and 4(b)]. Such a scenario arises naturally at asymmetric heterostructures, where intermixing with the top layer (SIO) or an incomplete surface termination (vacuum) is common. For the employed phenomenological model, the choice of two AH loops with slightly different coercive fields is fully compatible with the field and temperature dependence of the AHE [Figs. 3(c)–3(e)] and of the magnetization [Fig. 4(c)], as extracted from measurements of the magneto-optical Faraday effect [Fig. 4(d)]. In particular, comparing the magnetization loops for the two-coercive fields or single-coercive field AH model [Fig. 4(c)], one observes that it is nearly impossible to discern from the magnetization measurements the presence of two components with different switching fields, even when the two magnetizations have the same magnitude. We also point out that the assumption of two coercive fields for the AH two-channel model is not strictly needed for having a humplike Hall behavior when going through the switching field. Indeed, since the magnetization dependence of the intrinsic contribution to the AHE is generally nonlinear and not equivalent for the electronic

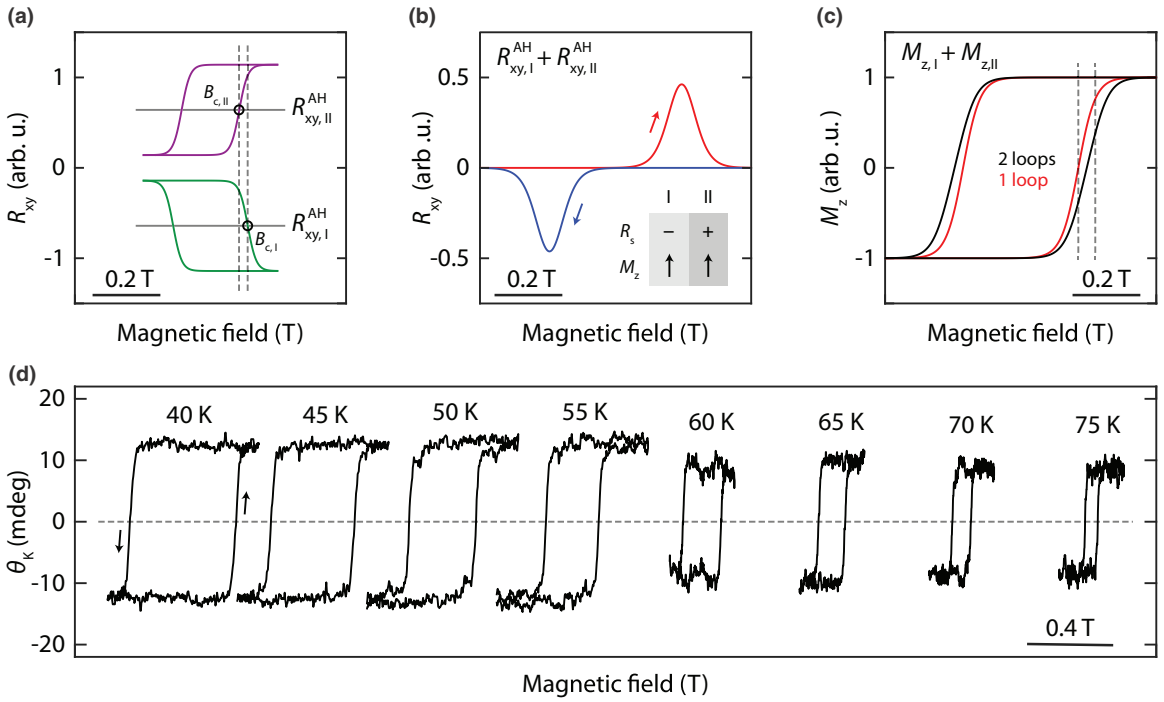

FIG. 4. Superposition of AH and magnetization loops. (a) Two separate (opposite) AH components as a function of the applied field and (b) the resulting total R^{AH}_{xy} for the case of two different coercive fields (indicated by the open circles). (c) Simulated magnetization profile as a function of the applied field, comparing a single loop with a double loop scenario. The two magnetization loops are extracted from the AH curves in (a) and are equal in magnitude. (d) Measured Faraday rotation angle as a function of the applied field for various temperatures ranging from 40 to 75 K. The curves are offset horizontally for visual clarity.

states having opposite sign Berry curvatures, then one can, in general, produce an imbalance with a humplike profile of the Hall response close to the magnetization switching point (see Sec. II E of the Supplemental Material [50]). The two-channel AH model should also be of relevance to other systems displaying the topological Hall effect, provided that a sign inversion is enabled by a temperature-dependent Hall response. It has also been proposed in the context of magnetically doped topological insulators [59].

IV. CONCLUSION

Finally, we discuss the scenario proposed here in the context of recent studies performed on SRO thin films and heterostructures, where similar anomalous Hall characteristics were observed and attributed to the topological Hall effect due to a skyrmion phase [19,29,60]. Although within this picture the topological Hall effect would be enhanced in the SIO/SRO/SIO case due to Dzyaloshinskii-Moriya interaction at both interfaces (contrary to our observation), our data cannot exclude contributions from real-space Berry curvature effects due to noncollinear spin textures forming in a specific range of temperature and magnetic fields. Our analysis highlights robust topological effects due to nontrivial Berry curvature in reciprocal space and that this scenario explains the superposition of AH components in asymmetric structures. We remark that, due to the strong connection between the magnetization and AHE, there is likely an interplay between noncollinear magnetism and the momentum-space Berry curvature. Hence, SRO-based heterostructures represent a unique platform to exploit and investigate the interplay of Berry curvature effects in both real and momentum space. The evolution of 3D Weyl points to pairs of topological bands in the 2D limit is a phenomenon that is not limited to ruthenates, but extends to magnetic t_{2g} systems in general. The same holds for the sensitivity of the total Berry curvature to interface effects and thus we expect that similar phenomenology would arise in other heterostructures based on ferromagnetic t_{2g} systems. In this respect, transition-metal oxides are an ideal platform owing to a delicate interplay between spin, charge, and lattice degrees of freedom. Our results establish that oxide interfaces host tunable topological phenomena, thereby providing new perspectives in the field of oxide electronics.

The data that support the findings of this study are available from the corresponding author upon reasonable request.

ACKNOWLEDGMENTS

The authors thank Y. Blanter, G. Koster, M. Golden, A. M. R. V. L. Monteiro, I. Lindfors-Vrejoiu, M. Gabay, J.-M. Triscone, S. Gariglio, and M. Kawasaki for discussions The authors thank M. Gibert for experimental support. This work was supported by The Netherlands Organisation for Scientific Research (NWO/OCW) as part of the Frontiers of Nanoscience (NanoFront) and VIDI program, by the Research Foundation Flanders (FWO, Belgium), and by the European Research Council under the European Union's Horizon 2020 programme/ERC Grant Agreements No. 677458, No. 770887, and No. 731473 (Quantox of QuantERA

ERA-NET Cofund in Quantum Technologies). C.A. and S.P. acknowledge financial support from Fondazione Cariplo via the project Magister (Project No. 2013-0726) and from CNR-SPIN via the Seed Project "CAMEO." C.A. acknowledges the CINECA award under the ISCRA initiative IsC54 "CAMEO" Grant, for the availability of high performance computing resources and support. W.B. acknowledges support by Narodowe Centrum Nauki (NCN, National Science Centre, Poland) Project No. 2016/23/B/ST3/00839. The work is supported by the Foundation for Polish Science through the IRA Programme co-financed by the European Union within SG OP. N.G. and J.V. acknowledge support from the GOA project "Solarpaint" of the University of Antwerp. The QuAnt-EM microscope was partly funded by the Hercules fund from the Flemish Government.

The authors declare no competing financial interests.

[1] M. V. Berry, Proc. R. Soc. London Ser. A **392**, 45 (1984).
[2] R. Karplus and J. Luttinger, Phys. Rev. **95**, 1154 (1954).
[3] K. Von Klitzing, Rev. Mod. Phys. **58**, 519 (1986).
[4] T. Jungwirth, J. Wunderlich, and K. Olejník, Nat. Mater. **11**, 382 (2012).
[5] N. Nagaosa, J. Sinova, S. Onoda, A. H. MacDonald, and N. P. Ong, Rev. Mod. Phys. **82**, 1539 (2010).
[6] S. Itoh, Y. Endoh, T. Yokoo, S. Ibuka, J.-G. Park, Y. Kaneko, K. S. Takahashi, Y. Tokura, and N. Nagaosa, Nat. Commun. **7**, 11788 (2016).
[7] G. Koster, L. Klein, W. Siemons, G. Rijnders, J. S. Dodge, C.-B. Eom, D. H. A. Blank, and M. R. Beasley, Rev. Mod. Phys. **84**, 253 (2012).
[8] Z. Fang, N. Nagaosa, K. S. Takahashi, A. Asamitsu, R. Mathieu, T. Ogasawara, H. Yamada, M. Kawasaki, Y. Tokura, and K. Terakura, Science **302**, 92 (2003).
[9] N. A. Sinitsyn, Q. Niu, J. Sinova, and K. Nomura, Phys. Rev. B **72**, 045346 (2005).
[10] S. Onoda, N. Sugimoto, and N. Nagaosa, Phys. Rev. Lett. **97**, 126602 (2006).
[11] Y. Kats, I. Genish, L. Klein, J. W. Reiner, and M. R. Beasley, Phys. Rev. B **70**, 180407(R) (2004).
[12] M.-H. Kim, G. Acbas, M.-H. Yang, M. Eginligil, P. Khalifah, I. Ohkubo, H. Christen, D. Mandrus, Z. Fang, and J. Cerne, Phys. Rev. B **81**, 235218 (2010).
[13] N. Haham, Y. Shperber, M. Schultz, N. Naftalis, E. Shimshoni, J. W. Reiner, and L. Klein, Phys. Rev. B **84**, 174439 (2011).
[14] S. J. Moon, H. Jin, K. W. Kim, W. S. Choi, Y. S. Lee, J. Yu, G. Cao, A. Sumi, H. Funakubo, C. Bernhard, and T. W. Noh, Phys. Rev. Lett. **101**, 226402 (2008).
[15] Y. F. Nie, P. D. C. King, C. H. Kim, M. Uchida, H. I. Wei, B. D. Faeth, J. P. Ruf, J. P. C. Ruff, L. Xie, X. Pan, C. J. Fennie, D. G. Schlom, and K. M. Shen, Phys. Rev. Lett. **114**, 016401 (2015).
[16] P. Schütz, D. Di Sante, L. Dudy, J. Gabel, M. Stübinger, M. Kamp, Y. Huang, M. Capone, M.-A. Husanu, V. N. Strocov, G. Sangiovanni, M. Sing, and R. Claessen, Phys. Rev. Lett. **119**, 256404 (2017).
[17] D. J. Groenendijk, C. Autieri, J. Girovsky, M. C. Martinez-Velarte, N. Manca, G. Mattoni, A. Monteiro, N. Gauquelin, J. Verbeeck, A. F. Otte, M. GabayS. Picozzi, and A. D. Caviglia, Phys. Rev. Lett. **119**, 256403 (2017).
[18] T. C. van Thiel, J. Fowlie, C. Autieri, N. Manca, M. Šiškins, D. Afanasiev, S. Gariglio, and A. D. Caviglia, ACS Mater. Lett. **2**, 389 (2020).
[19] Y. Ohuchi, J. Matsuno, N. Ogawa, Y. Kozuka, M. Uchida, Y. Tokura, and M. Kawasaki, Nat. Commun. **9**, 213 (2018).
[20] L. Wysocki, J. Schöpf, M. Ziese, L. Yang, A. Kovács, L. Jin, R. B. Versteeg, A. Bliesener, F. Gunkel, L. Kornblum *et al.*, ACS Omega **5**, 5824 (2020).
[21] Y. Gu, C. Song, Q. Zhang, F. Li, H. Tan, K. Xu, J. Li, M. S. Saleem, M. U. Fayaz, J. Peng *et al.*, ACS Appl. Mater. Interfaces **12**, 6707 (2020).
[22] D. Kan, T. Moriyama, and Y. Shimakawa, Phys. Rev. B **101**, 014448 (2020).
[23] P.-C. Wu, H. Song, Y. Yuan, B. Feng, Y. Ikuhara, R. Huang, P. Yu, C.-G. Duan, and Y.-H. Chu, Phys. Rev. Mater. **4**, 014401 (2020).
[24] B. Sohn, B. Kim, J. W. Choi, S. H. Chang, J. H. Han, and C. Kim, Current Appl. Phys. **20**, 186 (2020).
[25] Z. Y. Ren, F. Shao, P. F. Liu, M. X. Wang, J. K. Chen, K. K. Meng, X. G. Xu, J. Miao, and Y. Jiang, Phys. Rev. Appl. **13**, 024044 (2020).
[26] M. Ziese, L. Jin, and I. Lindfors-Vrejoiu, J. Phys.: Mater. **2**, 034008 (2019).
[27] Z. Li, S. Shen, Z. Tian, K. Hwangbo, M. Wang, Y. Wang, F. M. Bartram, L. He, Y. Lyu, Y. Dong *et al.*, Nat. Commun. **11**, 184 (2020).
[28] T. C. van Thiel, D. J. Groenendijk, and A. D. Caviglia, J. Phys.: Mater. **3**, 025005 (2020).
[29] J. Matsuno, N. Ogawa, K. Yasuda, F. Kagawa, W. Koshibae, N. Nagaosa, Y. Tokura, and M. Kawasaki, Sci. Adv. **2**, e1600304 (2016).
[30] S. Nakatsuji, N. Kiyohara, and T. Higo, Nature (London) **527**, 212 (2015).
[31] A. K. Nayak, J. E. Fischer, Y. Sun, B. Yan, J. Karel, A. C. Komarek, C. Shekhar, N. Kumar, W. Schnelle, J. Kübler, C. Felser, and S. S. P. Parkin, Sci. Adv. **2**, e1501870 (2016).
[32] P. K. Rout, P. V. Prakash Madduri, S. K. Manna, and A. K. Nayak, Phys. Rev. B **99**, 094430 (2019).
[33] B. Sohn, B. Kim, S. Y. Park, H. Y. Choi, J. Y. Moon, T. Choi, Y. J. Choi, T. W. Noh, H. Zhou, S. H. Chang, J. H. Han, and C. Kim, arXiv:1810.01615.
[34] L. Wang, Q. Feng, Y. Kim, R. Kim, K. H. Lee, S. D. Pollard, Y. J. Shin, H. Zhou, W. Peng, D. Lee *et al.*, Nat. Mater. **17**, 1087 (2018).
[35] D. Kan, T. Moriyama, K. Kobayashi, and Y. Shimakawa, Phys. Rev. B **98**, 180408(R) (2018).
[36] L. Wu, F. Wen, Y. Fu, J. H. Wilson, X. Liu, Y. Zhang, D. M. Vasiukov, M. S. Kareev, J. H. Pixley, and J. Chakhalian, arXiv:1907.07579.
[37] L. Wang, Q. Feng, H. G. Lee, E. K. Ko, Q. Lu, and T. W. Noh, Nano Lett. **20**, 2468 (2020).
[38] G. Kresse and J. Furthmüller, Comput. Mater. Sci. **6**, 15 (1996).

[39] G. Kresse and D. Joubert, Phys. Rev. B **59**, 1758 (1999).
[40] J. P. Perdew and A. Zunger, Phys. Rev. B **23**, 5048 (1981).
[41] D. M. Ceperley and B. J. Alder, Phys. Rev. Lett. **45**, 566 (1980).
[42] C. Etz, I. V. Maznichenko, D. Böttcher, J. Henk, A. N. Yaresko, W. Hergert, I. I. Mazin, I. Mertig, and A. Ernst, Phys. Rev. B **86**, 064441 (2012).
[43] S. Roy, C. Autieri, B. Sanyal, and T. Banerjee, Sci. Rep. **5**, 15747 (2015).
[44] C. Autieri, J. Phys.: Condens. Matter **28**, 426004 (2016).
[45] N. Marzari and D. Vanderbilt, Phys. Rev. B **56**, 12847 (1997).
[46] I. Souza, N. Marzari, and D. Vanderbilt, Phys. Rev. B **65**, 035109 (2001).
[47] A. A. Mostofi, J. R. Yates, Y.-S. Lee, I. Souza, D. Vanderbilt, and N. Marzari, Comput. Phys. Commun. **178**, 685 (2008).
[48] E. Grieten, O. Schalm, P. Tack, S. Bauters, P. Storme, N. Gauquelin, J. Caen, A. Patelli, L. Vincze, and D. Schryvers, J. Cultural Heritage **28**, 56 (2017).
[49] B. Conings, S. A. Bretschneider, A. Babayigit, N. Gauquelin, I. Cardinaletti, J. Manca, J. Verbeeck, H. J. Snaith, and H.-G. Boyen, ACS Appl. Mater. Interfaces **9**, 8092 (2017).
[50] See Supplemental Material at http://link.aps.org/supplemental/10.1103/PhysRevResearch.2.023404 for extended data and further details regarding *ab initio* calculations, magnetotransport, and structural characterization (see Refs. 61–73).
[51] D. Groenendijk, N. Manca, G. Mattoni, L. Kootstra, S. Gariglio, Y. Huang, E. van Heumen, and A. Caviglia, Appl. Phys. Lett. **109**, 041906 (2016).
[52] A. De Backer, K. Van den Bos, W. Van den Broek, J. Sijbers, and S. Van Aert, Ultramicroscopy **171**, 104 (2016).
[53] Q. Gan, R. Rao, C. Eom, J. Garrett, and M. Lee, Appl. Phys. Lett. **72**, 978 (1998).
[54] C. Jung, H. Yamada, M. Kawasaki, and Y. Tokura, Appl. Phys. Lett. **84**, 2590 (2004).
[55] D. Kan, R. Aso, H. Kurata, and Y. Shimakawa, J. Appl. Phys. **113**, 173912 (2013).
[56] T. Kobayashi, H. Tsuji, S. Tsunashima, and S. Uchiyama, Jpn. J. Appl. Phys. **20**, 2089 (1981).
[57] S. L. Zhang, Y. Liu, L. J. Collins-McIntyre, T. Hesjedal, J. Y. Zhang, S. G. Wang, and G. H. Yu, Sci. Rep. **3**, 2087 (2013).
[58] S. Zhang and T. Hesjedal, AIP Adv. **6**, 045019 (2016).
[59] K. M. Fijalkowski, M. Hartl, M. Winnerlein, P. Mandal, S. Schreyeck, K. Brunner, C. Gould, and L. W. Molenkamp, Phys. Rev. X **10**, 011012 (2020).
[60] B. Pang, L. Zhang, Y. B. Chen, J. Zhou, S. Yao, S. Zhang, and Y. Chen, ACS Appl. Mater. Interfaces **9**, 3201 (2017).
[61] C. Lichtensteiger, J. Appl. Cryst. **51**, 1745 (2018).
[62] J. M. D. Coey, M. Venkatesan, and P. Stamenov, J. Phys.: Condens. Matter **28**, 485001 (2016).
[63] Y. Tsema, M. Savoini, A. Tsukamoto, A. V. Kimel, A. Kirilyuk, and T. Rasing, Appl. Phys. Lett. **109**, 172403 (2016).
[64] N. Gauquelin, K. H. W. Van den Bos, A. Béché, F. F. Krause, I. Lobato, S. Lazar, A. Rosenauer, S. Van Aert, and J. Verbeeck, Ultramicroscopy **181**, 178 (2017).
[65] Z. Liao, M. Huijben, Z. Zhong, N. Gauquelin, S. Macke, R. J. Green, S. Van Aert, J. Verbeeck, G. Van Tendeloo, K. Held, G. A. Sawatzky, G. Koster, and G. Rijnders, Nature Mater. **15**, 425 (2016).
[66] A. I. Liechtenstein, V. I. Anisimov, and J. Zaanen, Phys. Rev. B **52**, R5467(R) (1995).
[67] Y. J. Chang, C. H. Kim, S.-H. Phark, Y. S. Kim, J. Yu, and T. W. Noh, Phys. Rev. Lett. **103**, 057201 (2009).
[68] C. Weingart, N. Spaldin, and E. Bousquet, Phys. Rev. B **86**, 094413 (2012).
[69] Z. Zhong, A. Tóth, and K. Held, Phys. Rev. B **87**, 161102 (2013).
[70] C. Autieri, M. Cuoco, and C. Noce, Phys. Rev. B **89**, 075102 (2014).
[71] T. Fukui, Y. Hatsugai, and H. Suzuki, J. Phys. Soc. Jpn. **74**, 1674 (2005).
[72] Z. Fang, K. Terakura, and N. Nagaosa, New J. Phys. **7**, 66 (2005).
[73] H. Zhang, H. Huang, K. Haule, and D. Vanderbilt, Phys. Rev. B **90**, 165143 (2014).